npj | systems biology and applications

Article

Published in partnership with the Systems Biology Institute

https://doi.org/10.1038/s41540-026-00675-6

Overcoming vascular niche–mediated TKI resistance in acute myeloid leukemia through miR-126 inhibition

Matthew Froid[1,2] ✉, Sergio Branciamore[3], Ziang Chen[3], David Frankhouser[3], Yu-Hsuan Fu[4], Jennifer Rangel Ambriz[3], Le Xuan Troung Nguyen[4], Jihyun Irizarry[4], Ya-Huei Kuo[4], Denis O'Meally[3], Bin Zhang[4], Guido Marcucci[4], Russell Rockne[3,5] & David Basanta[1,5] ✉

Acute myeloid leukemia (AML) is a hematologic malignancy originating in the bone marrow and often progressing to extramedullary sites. Despite advances in molecularly targeted therapies and hematopoietic stem cell transplantation, clinical outcomes remain poor. Tyrosine kinase inhibitors (TKIs) provide benefit to a subset of AML patients harboring FLT3-ITD mutations; however, relapse and resistance remain common. These therapeutic failures are driven by both intrinsic properties of leukemic stem cells (LSCs)—a quiescent, self-renewing population—and extrinsic cues from the tumor microenvironment. We previously demonstrated that arteriolar endothelial cells (ECs) produce miR-126, which is transferred to LSCs, promoting quiescence, treatment resistance, and niche retention. During disease progression, TNF-α secreted by expanding blasts suppresses EC miR-126 production. Following TKI administration, blast reduction lowers TNF-α levels, restoring EC miR-126 production, and this miR-126 expression enables LSCs to re-enter quiescence—thereby escaping therapy and facilitating relapse. To explore this dynamic, we developed an agent-based computational model of the AML bone marrow microenvironment, parameterized with in vitro and in vivo data. The model captures vascular niche remodeling and feedback between leukemic populations and endothelial signaling. Simulations reveal that LSC protection mediated by miR-126 can be disrupted by combining TKIs with miRisten, a miR-126 inhibitor. When administered on a defined schedule, this combination dismantles the protective niche and enhances LSC eradication. These findings underscore the therapeutic potential of targeting microenvironmental feedback to overcome resistance and prevent AML relapse.

Acute myeloid leukemia (AML) is an aggressive hematologic malignancy driven by genetic mutations, chromosomal aberrations, and epigenetic modifications that promote expansion of partially differentiated leukemic cells (blasts) that ultimately disrupt normal hematopoiesis[1]. Leukemia stem cells (LSCs), a primitive subpopulation of leukemic cells with unlimited self-renewal capacity and high treatment resistance, are responsible for the initiation and persistence of the disease and treatment failure[2–4]. Thus, a central strategy for achieving long-term remission and a cure in AML is LSC eradication. Although allogeneic stem cell transplantation can be curative and eliminates LSCs through a graft-versus-leukemia effect, its application is limited by substantial morbidity and mortality, making it unsuitable for elderly or medically unfit patients[5–7]. Therefore, the development of safer and more effective therapeutic approaches remains an urgent clinical priority for this disease.

Among the distinct molecular subtypes of AML, more than 20% of cases harbor an internal tandem duplication (ITD) mutation in the FLT3 gene (FLT3-ITD), which encodes a constitutively active mutant tyrosine kinase that drives leukemic growth[8,9]. The clinical benefit of integrating of

[1]Department of Integrated Mathematical Oncology, H. Lee Moffitt Cancer Center and Research Institute, Tampa, FL, USA. [2]The Cancer Biology PhD Program, University of South Florida, Tampa, FL, USA. [3]Department of Computational and Quantitative Medicine, Beckman Research Institute, City of Hope National Medical Center, Duarte, CA, USA. [4]Department of Hematologic Malignancies Translational Science, Gehr Family Center for Leukemia Research, Beckman Research Institute, City of Hope National Medical Center, Duarte, CA, USA. [5]These authors contributed equally: Russell Rockne, David Basanta.
✉e-mail: matthew.froid@moffitt.org; david@cancerevo.org

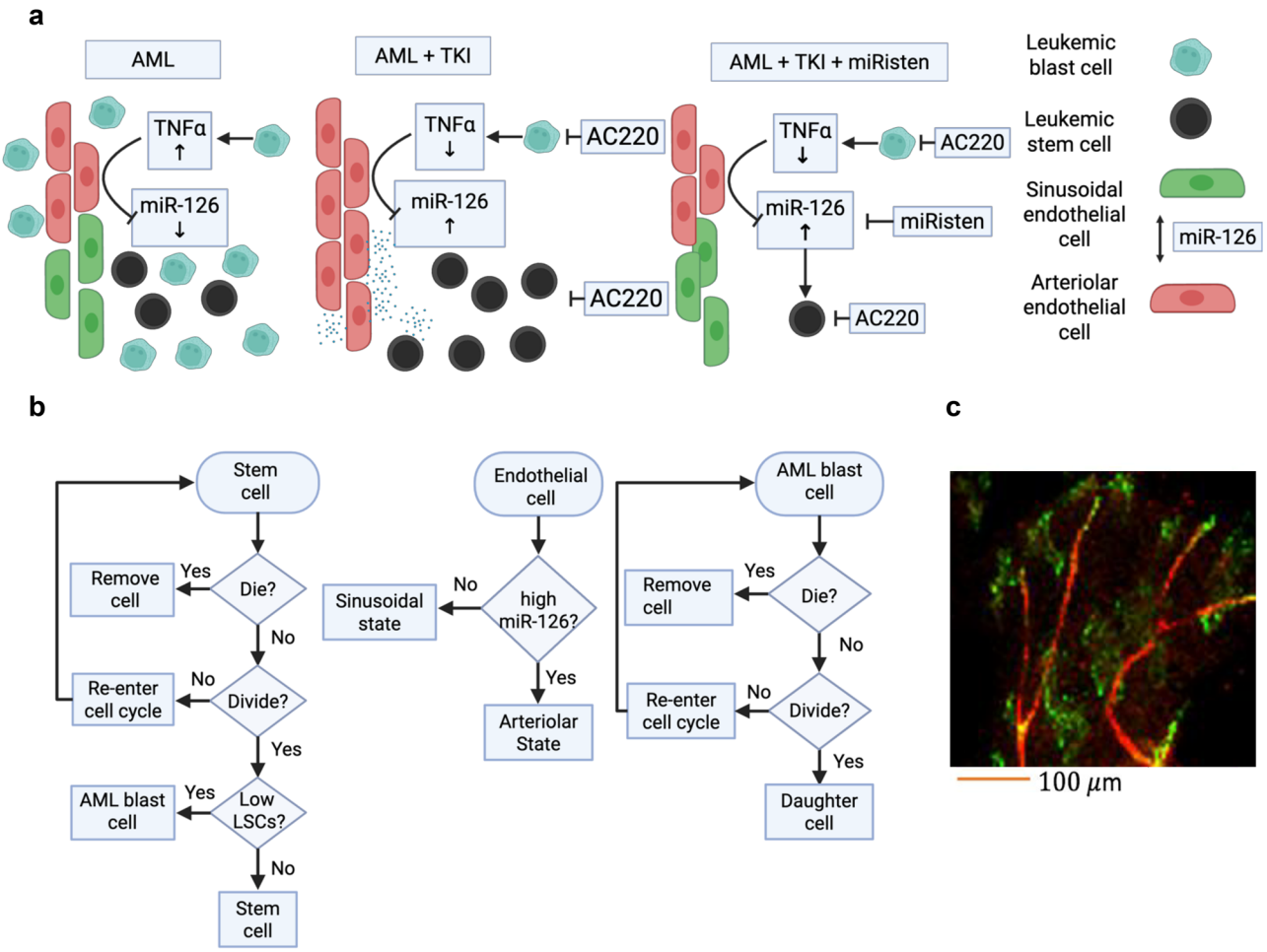

Fig. 1 | Conceptual and data-driven framework of the Janus phenomenon and vascular niche modeling. a Description of the Janus phenomena. **b** Flowcharts illustrating the sequence of actions taken by stem cells, blast cells, and endothelial cells. **c** Vascular data from a mouse tibia was used to construct the vascular architectures in the model. Red staining indicates ECs with higher miR-126 expression, while green staining indicates ECs with low miR-126 expression.

tyrosine kinase inhibitors (TKIs) into the treatment of FLT3-ITD AML has been demonstrated in several clinical trials[10–13]. However, TKI resistance emerges not only through mechanisms that are intrinsic to LSCs but also through the functional interplay of LSCs with the bone marrow (BM) tumor microenvironment (i.e., LSC niche)[14–16]. We previously reported that while cytotoxic treatment with TKIs initially induces cytoreduction of FLT3-ITD leukemic blasts, it also allows for arteriolar revascularization of the leukemic BM niche thereby resulting in LSC protection and paradoxically promoting disease relapse[15]. We identified miR-126 as a critical mediator of this dynamic process, as endothelial cell (EC) miR-126 regulates BM arteriolar revascularization supplied and is supplied by these vessels to LSCs, where it promotes homeostasis and quiescence.

MicroRNAs (miRNAs) are short non-coding RNAs that regulate gene expression by modulating target messenger RNA levels and regulating protein production. MiR-126 has been reported to contribute to LSC quiescence and treatment resistance[17]. This microRNA is highly produced in arteriolar ECs and exported to LSCs. During LSC-driven disease growth, the myeloblast progeny secretes pro-inflammatory cytokines, such as TNF-α, that suppress EC miR-126 production and, in turn, reduce the supply to LSCs which exit quiescence and ignite an accelerated leukemia growth[14–16,18]. However, upon initiation of cytoreductive therapy, the myeloblasts are killed, and the reduced TNF-α production causes a surge into EC miR-126 production and supply to LSCs. LSCs then retract into a quiescent and treatment-resistant state until the drug is cleared, upon which they restart another cycle of disease growth (i.e., relapse). This biphasic and paradoxical response to therapy, which ultimately leads to LSC persistence and disease relapse[15], exemplifies a treatment-related "Janus phenomenon" in AML (Fig. 1a), where the initial therapeutic benefit of leukemic blast reduction is offset by a detrimental, treatment-induced remodeling of the BM microenvironment and production of EC miR-126 protective of LSCs. To counteract the treatment-induced Janus phenomenon, we investigated miRisten, a novel miR-126 inhibitor[16], and hypothesized that optimization of timing and scheduling of miRisten administration in relation to TKI or other cytotoxic therapies may prevent the Janus phenomenon by reducing EC miR-126 production and supply to LSCs[14–16,19,20].

Mathematical modeling has been well established as an efficient method to test and predict novel multi-drug treatment strategies in cancer[21–24]. One such modeling method is agent-based modeling (ABM), a computational modeling approach where individual entities—called agents—operate based on defined rules that dictate how they interact with one another and their environment. These simulated interactions among autonomous agents allow for a better understanding of system-wide behaviors and outcomes. ABMs are inherently stochastic models built from the bottom up. The emergent effects, behavior that arises from the interactions of agents and their environments that isn't found in the parts themselves, often differ from those predicted by individual agent behaviors. The use of ABMs in cancer is well documented and facilitates an integrated approach to science in cancer[25]. The decision to use a more computational approach, such as an ABM over an ordinary differential equation (ODE)

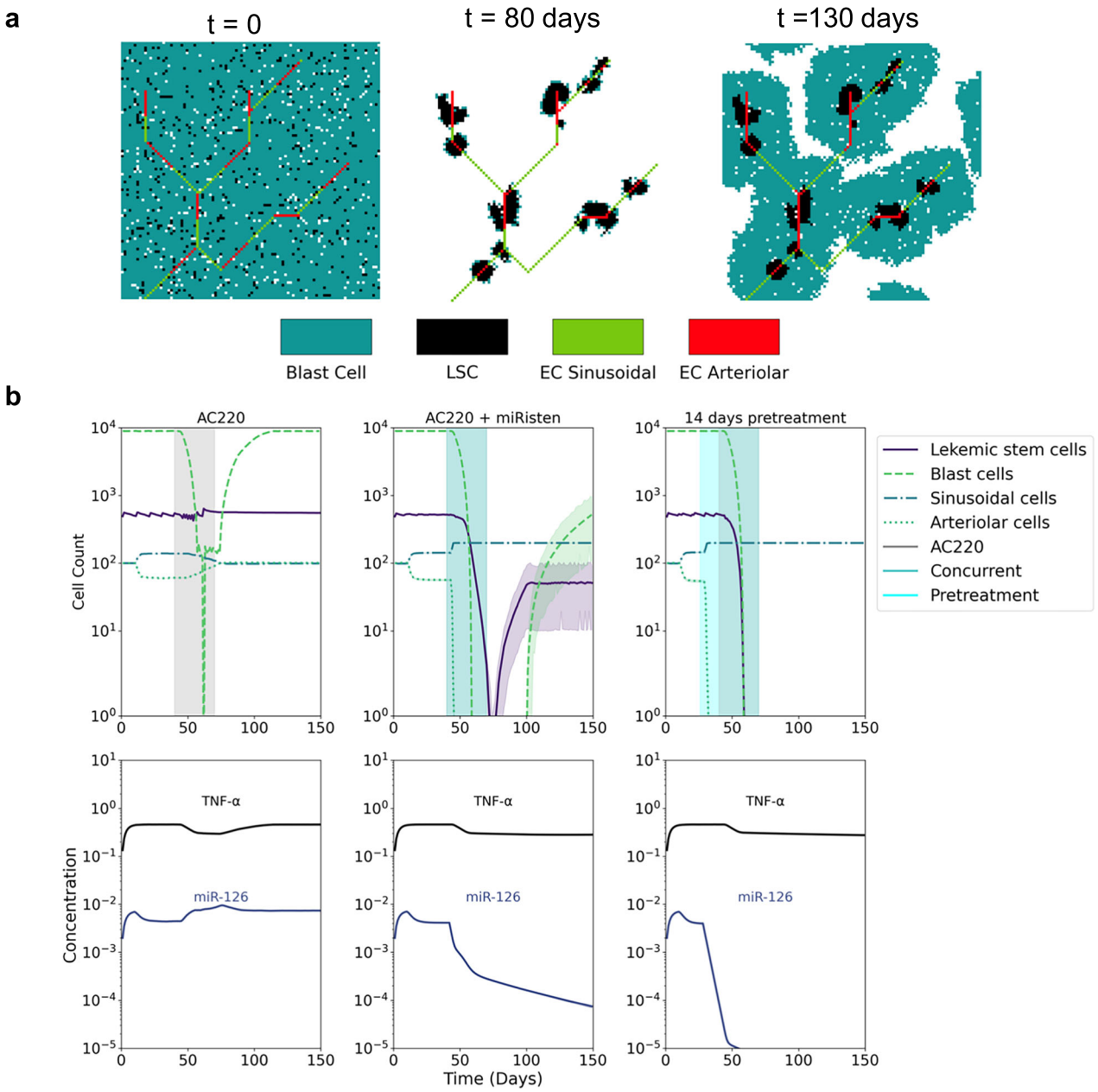

Fig. 2 | Spatial model dynamics under distinct treatment scheduling strategies. **a** Model visualizations taken from three timepoints. Cell population, TNF-α, and miR-126 results for the base vascular grid for three treatment conditions: **b** AC220 for 30 days, **c** AC220 + miRisten concurrently for 30 days, and **d** 14 days miRisten pretreatment followed by concurrent AC220 and miRsiten for 30 days.

was made due to the importance of spatial effects, which are lost in ODE models.

Here we leveraged tibial immunofluorescence staining to inform different vascular architectures[15], we developed an ABM to simulate the Janus phenomenon induced by TKIs and explore how different vascular architectures and drug schedules could lead to the elimination of LSCs and mitigate the risk of disease relapse. Our ABM was designed to replicate this phenomenon and suggests that the Janus effect in AML can be overcome through strategic treatment scheduling, such as pretreatment with miRisten followed by concurrent administration of a TKI and miRisten, or through sequential monotherapy with miRisten followed by a TKI (AC220). These findings not only underscore the pivotal roles of BM vascular dynamics and miR-126 in treatment resistance but also potentially lead to approaches that enhance the efficacy of FLT3-targeted therapies to eradicate LSCs and improve long-term outcomes in AML.

Results

The ABM Recapitulates the Janus Phenomenon in AML

Once calibrated, the ABM was first tested to determine its ability to recapitulate the Janus phenomena (Fig. 2a, b) with a vascular architecture intended to approximate generic blood vessel shapes in a two-dimensional space, with the only constraint that it must fit in the domain of the model. The ABM showed a decline of FLT3-ITD positive blast cells once TKI treatment with AC220 began, rapidly followed by reduction of blast-secreted TNF-α and in turn increased EC miR-126 levels. This led to LSCs expansion and eventually to blast regrowth once treatment ended. We observed that the EC populations shifted from a sinusoidal state characterized by miR-126^{low} ECs when TNF-α level was high, to an arteriolar state characterized by miR-126^{high} ECs when TNF-α level dropped due to blast cytoreduction. Thus, the ABM successfully recapitulated the Janus phenomenon, demonstrating that treatment-induced blast cytoreduction

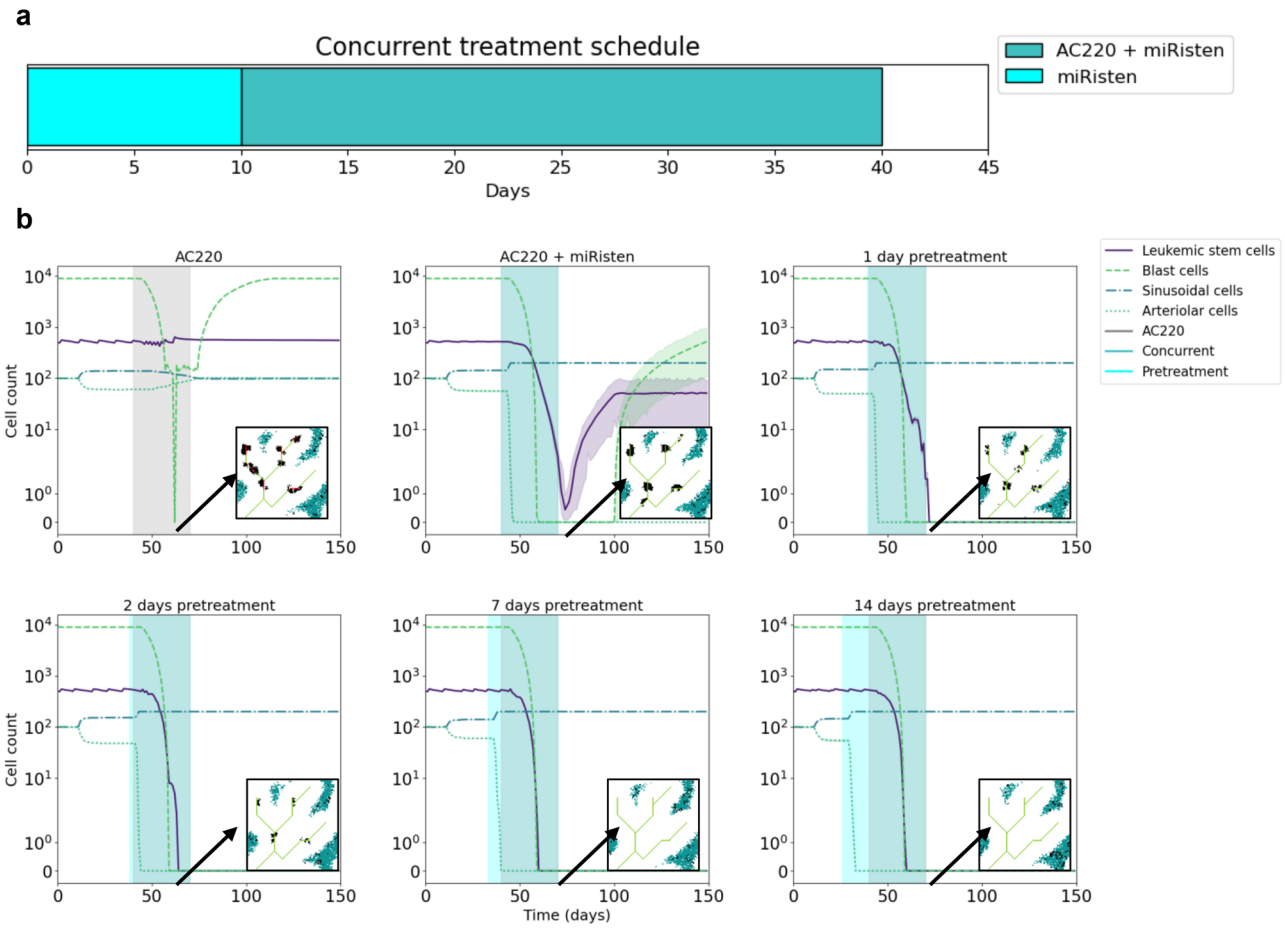

Fig. 3 | Treatment scheme and model outcomes for miR-126 pretreatment followed by combination therapy. a Treatment scheme for pretreatment with miRisten followed by combination AC220 and miRisten. **b** Results for the base vascular architecture for various combination periods. Inserts are taken at day 55, with AC220 starting at day 40 after the described pretreatment period.

resulted in TNF-α decrease and in turn in increased EC miR-126 production and enhanced density of arterioles that supply EC miR-126 to LSCs, which in turn expanded and drove leukemia regrowth (Fig. 2b).

The Janus Phenomenon can be overcome with different treatment schedules

Next, we asked if the Janus phenomenon could be mitigated with administration of miRisten, a novel oligonucleotide that inhibits mature miR-126[14–16,19,20]. When given simultaneously with AC220 (20 mg/kg/day), miRisten (10 mg/kg/day) decreased but did not completely eliminate disease (Fig. 2b). However, the model predicted that administration of miRisten alone for 14 days prior to the start of treatment with AC2202 alone or combination of AC220/miRisten could prevent disease relapse and progression.

With this data at hand and to determine the optimal duration for miRisten pretreatment, we next tested the ABM with various schedules of miRisten pretreatment, given 1 to 14 days before initiation of AC220 alone or AC220/miRisten combination (Fig. 3b). We observed that miRisten pretreatment, regardless of duration, was effective in reducing relapse and disease progression compared to AC220 or AC220/miRisten given without miR-126 pretreatment. When the total duration of miRisten pretreatment was limited to 30 days, a common duration of a treatment cycle for AML patients[26], a minimum of 2 days of miRisten pretreatment was required to prevent relapse if AC220 was then administered sequentially (Fig. 4b).

Treatment outcome depends on BM vascular architecture

To connect our ABM model to experimental data, we designed 16 different vascular architecture patterns, informed from in vivo data (Fig. 5a, b). For these 16 different vascular patterns, we tested the activity of pretreatment duration of miRisten followed by a combination of AC220 or miRisten/AC220 independently with no cross talk between each individual architecture (Fig. 5c). We found that for most vascular architectures, administering miRisten pretreatment followed by AC220 was more effective than miRisten pretreatment followed by AC220/miRisten, if the ultimate goal was to minimize total drug usage. However, when miRisten dosage was not considered as a limiting factor, the antileukemic activity was similar for miRisten pretreatment followed by AC220 alone or miRisten/AC220. It should also be noted that even though models with individual architectures resulted in disease cure at different timepoints, there was always a single time point at which cure was achieved regardless of the presence of vascular architecture. If no vascular architecture was present, then cure could not be reached. This can be viewed as the case when cells are to far away from vasculature to be reached by treatment. For the treatment regimen consisting of miRisten pretreatment followed by miRisten/AC220, cure was achieved with 2 days of miRisten pretreatment except for vascular architectures 4 and 8, where cure could be achieved with 1 day of miRisten pretreatment (Fig. 5c). Additionally, we noticed that the different vascular structures primarily fell into one of two groups, either lower ECs and slower response, or a higher number of ECs and a faster response (Fig. 5c). This is likely due to the number of ECs directly correlating to the amount of vasculature within the domain, with a more vascular domain allowing for a greater amount of both miRisten and AC220 to reach the entire domain. For the sequential regimen, when pretreatment was applied followed by only AC220, cure was achieved with as little as 1 day of miRisten pretreatment for all vascular architectures except for 6, which reached cure with 3 days of miRisten pretreatment (Fig. 5c).

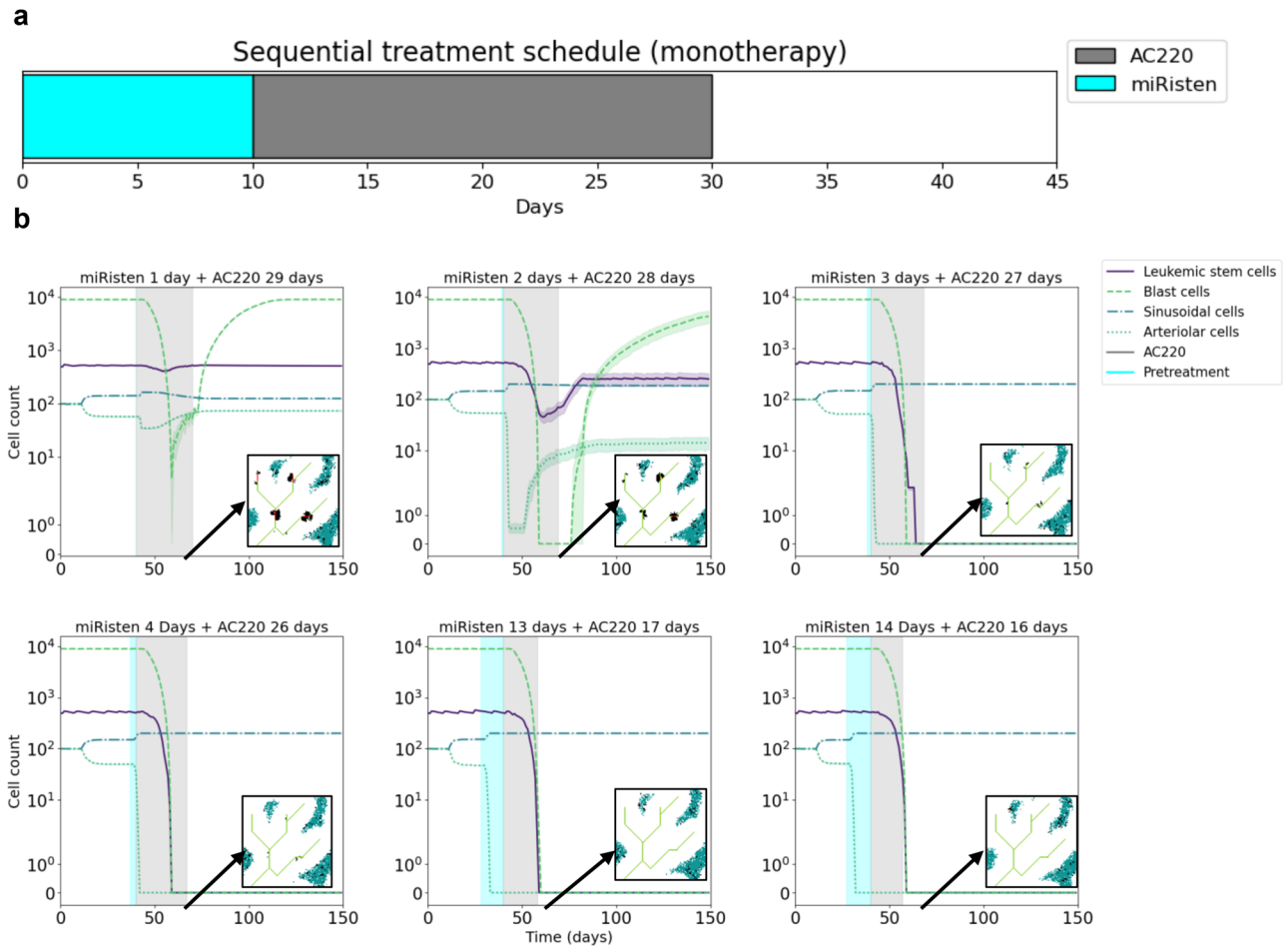

Fig. 4 | Treatment scheme and model outcomes for miR-126 pretreatment followed by monotherapy. a Treatment scheme for pretreatment with miRisten followed by only AC220. **b** Results for the base vascular architecture for various sequential monotherapy periods. Inserts are taken at day 55, with AC220 starting at day 40 after the described pretreatment period.

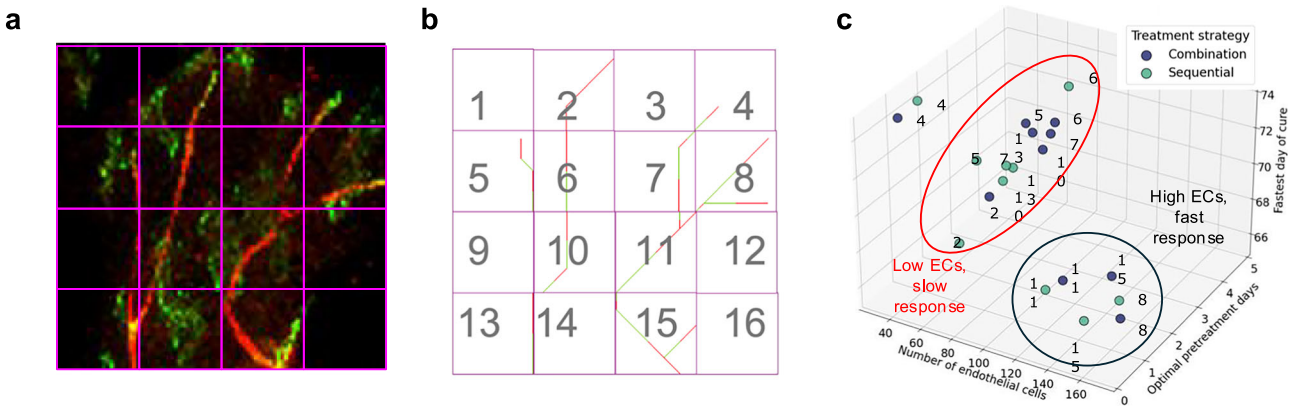

Fig. 5 | Vascular heterogeneity shapes optimal and fastest cure timepoints. a A section of mouse tibia was divided into 16 equal squares and used to inform the vascular architectures in the model. Red staining indicates ECs with higher miR-126 expression, while green staining indicates ECs with low miR-126 expression. **b** The vascular architecture designs in the model corresponding to the data in **a**. **c** 3D plot showing the relationship between number of ECs, optimal cure timepoint, and fastest cure timepoint (z-axis).

Distance of LSCs from vessels impact on disease response

Noticing that there was a difference in response for some of the vascular architectures to miRisten pretreatment followed by AC220 or miRisten/AC220, we sought to explore if the spatial configuration of the vascular architectures could impact LSC resistance in the respective BM niches. Thus, we counted the mean number of surviving LSCs clones based off their distance from the vasculature at the final timestep in the model (Fig. 6a–d, Supplemental Figs. 1–2), where a clone referres to cells derived from a single LSC. All progeny cells were computationally tracked over time, allowing for analysis of spatial dynamics, such as their proximity to vasculature and survival outcomes under different treatment conditions. We observed that for most vascular architectures, pretreatment with miRisten for 1 day followed by 29 days of AC220 significantly reduced the number of LSCs through miR-126 inhibition by miRisten removing the protective vascular

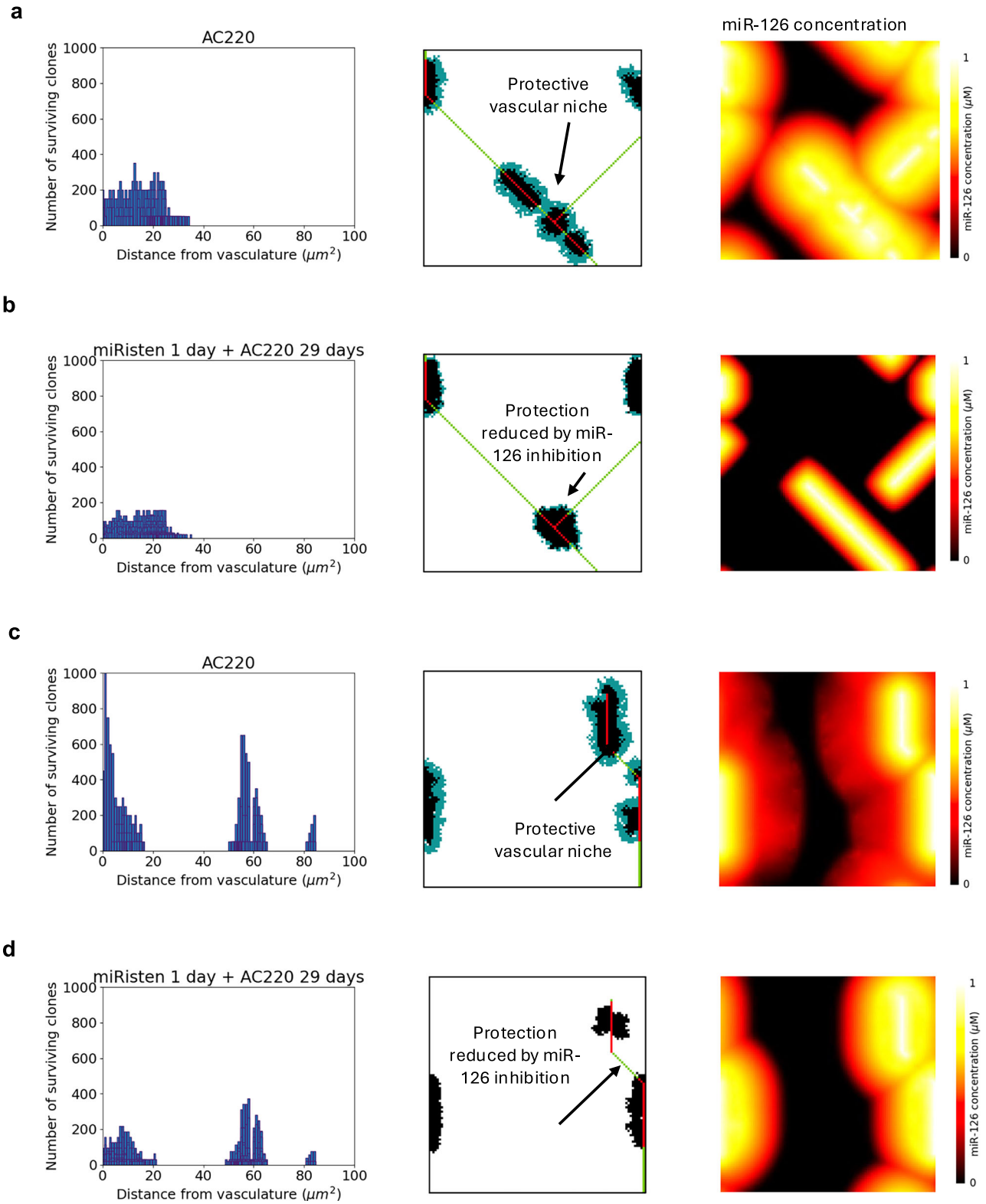

Fig. 6 | Architecture-specific effects of miR-126 pretreatment on treatment response. a Vascular architecture #15 at timepoint 80, 10 days after treatment AC220 alone. **b** Vascular architecture #15 at timepoint 80, 10 days after 1 day miRisten pretreatment and 29 days of AC220. **c** Vascular architecture #5 at timepoint 80, 10 days after treatment AC220 alone. **d** Vascular architecture #5 at timepoint 80, 10 days after 1 day miRisten pretreatment and 29 days of AC220.

niche (Fig. 6a–d, Supplemental Figs. 1–2). With this data at hand, we then focused on the spatial distribution of surviving clones (Fig. 6a–d, Supplemental Figs. 1–2). We observed that in vascular configuration #15, all surviving clones were situated relatively close to the vessels (less than 25 μm^2), according to the hypothesis that LSC homeostasis is supported by local vascular miR-126 supply[14,15]. Of note, for a system configuration with no vasculature, it was impossible to achieve cure as no drug could be delivered.

We observed that for all vascular configurations when miRisten pretreatment was followed by AC220, there were less surviving LSCs closer to the vessels than those surviving when no miRisten pretreatment was given

and AC220 alone was administered (Fig. 6a–d, Supplemental Figs. 1–2a–l). This observation supports the hypothesis that LSC distance from vasculature is a critical determinant of therapy activity. However, we identified a specific treatment timepoint where miRisten pretreatment significantly reduced the Janus phenomenon. This suggests that precise timing of miRisten administration can help mitigate adverse spatial effects on LSC response.

Discussion

Herein, we demonstrated that an ABM of the BM microenvironment calibrated with experimental data recapitulated a Janus phenomenon in AML[16]. Initial findings revealed that EC miR-126 production increased upon administration of cytotoxic therapy due to depletion of TNF-α producing myeloblasts. Decrease in TNF-α resulted in a surge in EC miR-126 production, increased arteriolar vascularization and enhanced EC miR-126 supply to LSCs, which in turn retracts in quiescence and becomes invulnerable to treatment, posing the basis for future disease relapse. Preventing EC miR-126 production with miR-126 inhibition with miRisten mitigated the paradoxical remodeling of the BM vasculatures that, during cytotoxic treatment, provides LSC protection that we called the Janus phenomenon. Pretreatment with miRisten followed by treatment with AC220 or miRisten/AC220 captured optimal dose schedules that prevented disease relapse while minimizing the amount of drugs given. This model conceptually validates our previous experimental findings and underscores the usefulness of ABMs in understanding how to mitigate optimize drug schedule and delivery in AML[14–16].

Analysis of 16 different vascular patterns informed by experimental data revealed that pretreatment with miRisten followed by either concurrent miRisten/AC220 or AC220 alone, prevented relapse under specific conditions, although not equivalent. Spatial analysis of LSC survival revealed the role of vascular structures in protecting LSCs from the cytotoxic effects of therapy (Fig. 6a–d). While there is no exact minimal distance from the vasculature that shelters the LSCs across all vascular architectures in the model, we did notice that the closer to the vessel the LSCs were located, the more the protective effect of EC miR-126. We recognize there are some limitations with the implementation of vascular architectures in this model. While most tissues are perfused to some extent, the assumption of an entirely avascular domain is intended to model localized microenvironments within the BM where vascular access is severely restricted. In the context of AML, leukemic cells have been shown to colonize hypoxic or poorly vascularized niches, particularly in regions distant from endosteal or sinusoidal vessels. These localized zones can experience significantly reduced oxygen and drug penetration, effectively functioning as avascular compartments from the perspective of therapeutic exposure[27,28]. Additionally, our data support this notion, as we observe avascular regions in the mouse tibia used to inform the model. Our model simplifies this biological reality by representing such niches as fully avascular domains to isolate and examine the effects of limited drug accessibility and spatial crowding. This abstraction enables us to evaluate worst-case scenarios in drug delivery, which are critical for understanding mechanisms of treatment resistance and relapse dynamics. Future work may explore hybrid domains with spatially varying vascularization and angiogenesis to capture more complex tissue structures and the dynamic interplay between the treatments and BM remodeling.

Importantly, our simulations identified a quantifiable window of optimal miRisten pretreatment duration. Across the majority of vascular architectures tested, at least 2–3 days of miRisten pretreatment were required to sufficiently suppress endothelial miR-126 and prevent the rebound in vascular protection observed during TKI administration. Shorter pretreatment intervals failed to deplete miR-126 signaling adequately before cytotoxic therapy began, whereas longer intervals offered no additional benefit. Thus, our model predicts that a defined period of miRisten pretreatment—approximately 3 days—is sufficient to mitigate the Janus phenomenon while minimizing total drug exposure.

These insights emphasize the spatial dependency of therapeutic efficacy, where proximity to vasculature significantly affects the potential success of anticancer therapy in eradicating AML. Thus, our study provides a computational framework for understanding how vascular architectures and treatment timing synergistically impact outcomes that matches the experimental observation and allows for exploration of other therapeutic strategies that target the complex interplay between BM microenvironment and LSCs. Of note, although it is impossible to determine the precise vascular architectures in patients, we show that there may be a minimum number of days of miRisten pretreatment that can mitigate the Janus phenomenon for most vascular architectures in the BM microenvironment. This could pave the way for future advances in AML personalized treatment, where combination therapies are used to mitigate treatment response for a variety of geometrical and structural features of the BM niche. In fact, beyond AML and TKIs, our findings may have broader therapeutic implications for other hematologic malignancies that exhibit stem cell persistence and microenvironment-mediated resistance, as well as other treatment modalities, such as BCL-2 inhibitors[29] or immune-based interventions where microenvironment-driven resistance may play a significant role. Similar modeling approaches could also be extended to solid tumors where the vascular niche may play a similar protective role in cancer stem cells' survival.

A key strength of this study is the integration of computational modeling with experimental vascular architectures, allowing for hypothesis-driven exploration of combination treatment strategies in silico. The ABM enables spatially explicit simulations that capture heterogeneity in therapeutic response due to vascular proximity, a factor difficult to assess in traditional preclinical models. This methodology could be extended to study other microenvironmental interactions, such as stromal-mediated drug resistance or immune evasion mechanisms in cancer. However, like all computational models, our approach has limitations. The ABM is constrained by predefined assumptions regarding cell behavior, vascular dynamics, and the production, decay, and diffusion of molecules in the tissue. Additionally, while our vascular structures were informed by experimental data, they are two-dimensional simplifications of complex and heterogeneous three-dimensional tissues. Future refinements should include angiogenesis, differential response of LSCs and blast cells to TKIs, and other treatment combinations.

Our findings highlight the importance of vascular architecture in shaping AML treatment responses and propose a strategy for mitigating the Janus phenomenon through miRisten pretreatment. By integrating computational modeling with experimental data, this study provides a foundation for optimizing treatment timing and microenvironment-targeted therapies. Further experimental and clinical validation will be essential to translate these insights into patient care, potentially improving outcomes for AML patients.

Methods

Agent Based Model of the AML BM Microenvironment

The ABM was built on the Hybrid Cellular Automata (HCA) paradigm applied to study evolutionary dynamics and cellular interactions in various biological contexts[30–37]. An HCA framework is defined by discrete agent types updated at each time step based on flowcharts and partial differential equations describing the dynamics of signaling molecules in the microenvironment. The model was implemented using the Hybrid Automata Library (HAL)[38]. Here, the model has four types of agents, representing blast cells, LSCs, and ECs representing vasculature. The model contains four diffusible molecules, miR-126, TNF-α, a miR-126 inhibitor, miRisten, and an FLT3 TKI, AC220. In the sections below we will describe the interactions between cell types and diffusible within the same environment.

Model Initial Conditions Agent and Molecule Rules

The model is defined on a 2D rectangular grid (100 × 100 pixels) representing a section of the AML BM niche, where each pixel represents 10 μm^2 and each timestep represents one 24-hour period. When the model is

initialized, all cells are placed on the grid randomly, except for the ECs, which are structured based on experimental data. For each timestep, one cell is chosen randomly to perform its actions (Fig. 1). The initial population fractions and division rates were informed from experimental data, and the model is initialized with 90% of the domain containing blast cells, 5% of the domain consisting of LSCS, and a maximum of 2% of the domain consisting of ECs literature (Supplementary Table 1)[39]. For the domains when we are considering different vascular architectures, these were informed from previously published experimental data[15].

Blast Cells

AML blast cells are modeled on a 2-D lattice and updated using discrete timesteps. At each timestep, cell death and division are evaluated as independent Bernoulli events. For each AML blast cell, death occurs with a per-timestep death probability. This is implemented by drawing a random number from a uniform distribution $U(0, 1)$; if the value is less than the death probability, the cell undergoes apoptosis and is removed from the system. If the cell survives the death check, it may divide with a per-timestep division probability. Division is spatially constrained by a Moore neighborhood (the eight horizontally, vertically, and diagonally adjacent sites). If at least one neighboring lattice site is empty, a single daughter cell is placed at random into one of the available locations. If no empty sites exist, division is aborted due to space limitation. This implementation represents stochastic, asynchronous death and proliferation at the single-cell level, with biological rates approximated as constant per-timestep probabilities[15].

Leukemic Stem Cells (LSCs)

LSCs also divide once per 24-hour period and follow a similar decision-making process to the blast cells, with added complexity. Spatial constraints for the LSC division are also defined using a Moore neighborhood, where each cell evaluates the eight adjacent sites for available space. If space is available, the LSC may divide, placing a daughter cell into one of the empty neighboring positions. If the LSC does not divide, it re-enters the cell cycle and remains an LSC. If it dies, it is removed from the system. Upon division, an LSC can produce either another LSC (symmetric division) or an AML blast cell (asymmetric division), depending on the current LSC population. Specifically, if the number of LSCs falls below 5% of the domain—representing their initial abundance—division yields another LSC to maintain the stem cell pool. Otherwise, the daughter cell is an AML blast. LSCs also experience natural apoptosis, though at a lower probability than blast cells, and it also follows an identical Bernoulli process for cell death. This probabilistic rule set enables the model to simulate the hierarchical organization of AML and the role of LSCs in sustaining both the stem and progenitor compartments[40,41].

ECs

The ABM was initially investigated with a generic vascular structure, and then 16 additional vascular structures were considered, informed by experimental data (Fig. 1c). The vasculature was assumed to be fixed and are represented by ECs. The ECs are assumed to transition between two distinct states based on the presence of miR-126. If the local miR-126 concentration is higher than the TNF-α, the EC adopts a miR-126-producing arteriolar state. Conversely, if the miR-126 concentration is lower than the TNF-α concentration, the cell assumes a sinusoidal state, where it does not produce miR-126. This binary state reflects the ECs adaptability and its potential involvement in vascular remodeling and microenvironment regulation. We are not assuming ECs divide, as modeling angiogenesis would increase the computational complexity of the model.

Diffusible molecules and drugs

All diffusible species in the model—TNF-α, miR-126, AC220, and miRisten—were modeled with partial differential equations (PDEs) describing production, diffusion, and decay (Eq. 1). The concentration of each molecule was produced, decayed, and passively transported through the domain according to

$$\frac{\partial C(x,y,t)}{\partial t} = \underbrace{D_C\left(\frac{\partial^2 C}{\partial x^2} + \frac{\partial^2 C}{\partial y^2}\right)}_{\text{Diffusion}} + \underbrace{\alpha_C S}_{\text{Production}} - \underbrace{\delta_C C}_{\text{Decay}} \quad (1)$$

where C is the concentration of the diffusible, S is the source of the diffusible, D is the diffusion coefficient, α_C is the basal production of the molecule, and δ_C is the clearance, or decay, of the molecule. Parameter values were estimated based on the molecular weight of each diffusible as well as approximating the distance the molecule would travel through a space similar in size to the domain of the model in one 24-hour period, the size of the timestep used in the model (Supplementary Table 1). The system of PDEs was solved using the forward time and space-centered space scheme, with periodic boundary conditions in HAL.

TNF-α and miR-126

TNF-α was expressed and diffused from blast cells, while miR-126 diffused from the ECs, both following Eq. 1. Additionally, local levels of miR-126 also impacted the LSC compartment. When the local area around an LSC contained an amount of miR-126 higher than that of the base TNF-α concentration, LSCs had decreased sensitivity to AC220, resulting in little to no death of the LSCs due to AC220. For each vascular architecture and treatment condition, 50 simulations were run.

TNF-α and miR-126 are produced by the blast cells and ECs respectively at a basal rate of 0.20 μM per timestep for miR-126 and 0.15 μM per timestep for TNF-α. These values were inferred computationally based on the molecular weight of the molecules and how quickly they could move through a space the size of the model domain in one 24-hour period. We assume that blasts and ECs produce TNF-α and miR-126 respectively at constant rates, unless miR-126 is inhibited by TNF-α or miRisten.

AC220 and miRisten

Both drugs, AC220 (a representative TKI) and miRisten, diffused through the domain originating from the vasculature, according to a transport PDE similar to TNF-α and miR-126. Blast and stem cells uptake AC220, and the probability of death increases proportional to the amount of AC220[26,42–44]. For LSCs, the AC220-induced increase in death probability is also impacted by the local concentration of miR-126. If miR-126 is higher than that of AC220, there is no increase in death probability from AC220. Treatment-induced cytotoxic effects of AC220 on blast cells and LSCs were inferred computationally through comparing model outputs with published data. More specifically, the basal death rates of the blast cells and LSCs are increased based on the concentration of AC220 taken up by each cell. The suppressive effects of miRisten on miR-126 by EC cells were done in a similar manner [15,26,39] AC220 and miRisten treatments are delivered via the vasculature once per day.

Visualization and Analysis

Python version 3.11.17 was used for all data processing, analysis, and visualization. BioRender was used to generate illustrations in some of the figures.

Statistical Support and Reproducibility

To account for the stochastic nature of the model, all simulations were run for 50 independent iterations. This repetition ensured a sufficiently large sample size and allowed for the assessment of variability across runs. A formal power analysis was not conducted, as is typical in agent-based modeling studies, due to the exploratory nature of the simulations and the ability to generate arbitrarily large synthetic datasets. Instead, we relied on multiple iterations (n = 50) to characterize the variability and robustness of outcomes arising from the model's inherent stochasticity.

To ensure reproducibility of results, each simulation was initialized with a fixed random seed.

Data availability

Source code can be found at https://github.com/mfroid/JanusABM. Due to storage limitations caused by the large size of the data generated for this study, all random seeds used to generate the data are available in the GitHub repository.

Received: 10 July 2025; Accepted: 12 February 2026;
Published online: 19 March 2026

References

1. Shafat, M. S. et al. The bone marrow microenvironment–Home of the leukemic blasts. *Blood Rev.* **31**, 277–286 (2017).
2. Bonnet, D. & Dick, J. E. Human acute myeloid leukemia is organized as a hierarchy that originates from a primitive hematopoietic cell. *Nat. Med.* **3**, 730–737 (1997).
3. Chen, Y. et al. The genesis and evolution of acute myeloid leukemia stem cells in the microenvironment: from biology to therapeutic targeting. *Cell Death Discov.* **8**, 397 (2022).
4. Dick, J. E. Acute myeloid leukemia stem cells. *Ann. N. Y. Acad. Sci.* **1044**, 1–5 (2005).
5. Bewersdorf, J. P. et al. Outcomes of allogeneic hematopoietic cell transplantation in patients with myelofibrosis—a systematic review and meta-analysis. *Transplant. Cell. Ther.* **27**, 873. e1–873 (2021).
6. Kassim, A. A. & Savani, B. N. Hematopoietic stem cell transplantation for acute myeloid leukemia: a review. *Hematol./Oncol. Stem Cell Ther.* **10**, 245–251 (2017).
7. Rashidi, A. et al. Outcomes of allogeneic stem cell transplantation in elderly patients with acute myeloid leukemia: a systematic review and meta-analysis. *Biol. Blood Marrow Transplant.* **22**, 651–657 (2016).
8. Lagunas-Rangel, F. A. DNA damage accumulation and repair defects in FLT3-ITD acute myeloid leukemia: implications for clonal evolution and disease progression. *Hematol. Oncol.* **41**, 26–38 (2023).
9. Yanada, M. et al. Prognostic significance of FLT3 internal tandem duplication and tyrosine kinase domain mutations for acute myeloid leukemia: a meta-analysis. *Leukemia* **19**, 1345–1349 (2005).
10. Allert, C. et al. Protein tyrosine kinase 2b inhibition reverts niche-associated resistance to tyrosine kinase inhibitors in AML. *Leukemia* **36**, 2418–2429 (2022).
11. Knight, T. E. et al. FLipping" the story: FLT3-mutated acute myeloid leukemia and the evolving role of FLT3 inhibitors. *Cancers* **14**, 3398 (2022).
12. Loschi, M. et al. FLT3 tyrosine kinase inhibitors for the treatment of fit and unfit patients with FLT3-mutated AML: a systematic review. *Int. J. Mol. Sci.* **22**, 5873 (2021).
13. Negotei, C. et al. A review of FLT3 kinase inhibitors in AML. *J. Clin. Med.* **12**, 6429 (2023).
14. Zhang, B. et al. Bone marrow niche trafficking of miR-126 controls the self-renewal of leukemia stem cells in chronic myelogenous leukemia. *Nat. Med.* **24**, 450–462 (2018).
15. Zhang, B. et al. Treatment-induced arteriolar revascularization and miR-126 enhancement in bone marrow niche protect leukemic stem cells in AML. *J. Hematol. Oncol.* **14**, 1–19 (2021).
16. Zhang, L. et al. Targeting miR-126 in inv (16) acute myeloid leukemia inhibits leukemia development and leukemia stem cell maintenance. *Nat. Commun.* **12**, 6154 (2021).
17. Lechman, E. R. et al. miR-126 regulates distinct self-renewal outcomes in normal and malignant hematopoietic stem cells. *Cancer Cell* **29**, 214–228 (2016).
18. Epstein, S. E. et al. Janus phenomenon: the interrelated tradeoffs inherent in therapies designed to enhance collateral formation and those designed to inhibit atherogenesis. *Circulation* **109**, 2826–2831 (2004).
19. Qiao, J. et al. Targeting miR-126 in ph+ acute lymphoblastic leukemia. *Leukemia* **37**, 1540–1544 (2023).
20. Wang, H. et al. Targeting miR-126 disrupts maintenance of myelodysplastic syndrome stem and progenitor cells. *Clin. Transl. Med.* **11**, e610 (2021).
21. Araujo, A. et al. Quantification and optimization of standard-of-care therapy to delay the emergence of resistant bone metastatic prostate cancer. *Cancers* **13**, 677 (2021).
22. Bishop, R. T. et al. The bone ecosystem facilitates multiple myeloma relapse and the evolution of heterogeneous drug resistant disease. *Nat. Commun.* **15**, 2458 (2024).
23. Gallaher, J. et al. Improving treatment strategies for patients with metastatic castrate resistant prostate cancer through personalized computational modeling. *Clin. Exp. Metastasis* **31**, 991–999 (2014).
24. Macklin, P. et al. *P*atient-calibrated agent-based modelling of ductal carcinoma in situ (DCIS): from microscopic measurements to macroscopic predictions of clinical progression. *J. Theor. Biol.* **301**, 122–140 (2012).
25. West, J., Robertson-Tessi, M. & Anderson, A. R. Agent-based methods facilitate integrative science in cancer. *Trends Cell Biol.* **33**, 300–311 (2023).
26. Zarrinkar, P. P. et al. AC220 is a uniquely potent and selective inhibitor of FLT3 for the treatment of acute myeloid leukemia (AML). *Blood, J. Am. Soc. Hematol.* **114**, 2984–2992 (2009).
27. Bruno, S. et al. The role of hypoxic bone marrow microenvironment in acute myeloid leukemia and future therapeutic opportunities. *Int. J. Mol. Sci.* **22**, 6857 (2021).
28. Passaro, D. et al. Increased vascular permeability in the bone marrow microenvironment contributes to disease progression and drug response in acute myeloid leukemia. *Cancer Cell* **32**, 324–341 (2017).
29. Pollyea, D. et al. Erratum: venetoclax for AML: changing the treatment paradigm. *Blood Adv.* **3**, 4326–4335 (2019).
30. Anderson, A. R. A hybrid mathematical model of solid tumour invasion: the importance of cell adhesion. *Math. Med. Biol. J. IMA* **22**, 163–186 (2005).
31. Anderson, A. R. et al. Tumor morphology and phenotypic evolution driven by selective pressure from the microenvironment. *Cell* **127**, 905–915 (2006).
32. Araujo, A. et al. An integrated computational model of the bone microenvironment in bone-metastatic prostate cancer. *Cancer Res.* **74**, 2391–2401 (2014).
33. Araujo, A. et al. Size matters: metastatic cluster size and stromal recruitment in the establishment of successful prostate cancer to bone metastases. *Bull. Math. Biol.* **80**, 1046–1058 (2018).
34. Colyer, B. et al. A seven-step guide to spatial, agent-based modelling of tumour evolution. *Evolut. Appl.* **17**, e13687 (2024).
35. Cook, L. M. et al. Predictive computational modeling to define effective treatment strategies for bone metastatic prostate cancer. *Sci. Rep.* **6**, 29384 (2016).
36. Metzcar, J. et al. A review of cell-based computational modeling in cancer biology. *JCO Clin. Cancer Inform.* **2**, 1–13 (2019).
37. Stephan, S. et al. Agent-based approaches for biological modeling in oncology: A literature review. *Artif. Intell. Med.* **152**, 102884 (2024).
38. Bravo, R. R. et al. Hybrid automata library: a flexible platform for hybrid modeling with real-time visualization. *PLoS Comput. Biol.* **16**, e1007635 (2020).
39. Akinduro, O. et al. Proliferation dynamics of acute myeloid leukaemia and haematopoietic progenitors competing for bone marrow space. *Nat. Commun.* **9**, 1–12 (2018).
40. Chao, S., Yan, H. & Bu, P. Asymmetric division of stem cells and its cancer relevance. *Cell Regener.* **13**, 5 (2024).
41. Stahl, M., Kim, T. K. & Zeidan, A. M. Update on acute myeloid leukemia stem cells: new discoveries and therapeutic opportunities. *World J. Stem Cells* **8**, 316 (2016).

42. Cao, S., Wang, Q. & Zhu, G. From chemotherapy to targeted therapy: unraveling resistance in acute myeloid leukemia through genetic and non-genetic insights. *Int. J. Mol. Sci.* **26**, 4005 (2025).
43. Capelli, D. FLT3-mutated leukemic stem cells: mechanisms of resistance and new therapeutic targets. *Cancers* **16**, 1819 (2024).
44. Murphy, L. A. & Winters, A. C. Emerging and future targeted therapies for pediatric acute myeloid leukemia: targeting the leukemia stem cells. *Biomedicines* **11**, 3248 (2023).

Acknowledgements

Research reported in this publication was supported in part by Robert and Lynda Altman Family Foundation and included work supported by the City of Hope Integrative Genomics Core, High Performance Research Computing Center and Biostatistics and Mathematical Oncology shared resources supported by the National Cancer Institute of the National Institutes of Health under grant numbers P30CA033572, U01CA250046, U01CA293853, R01CA290007 and U01CA244101. The content is solely the responsibility of the authors and does not necessarily represent the official views of the National Institutes of Health. MF and DB acknowledge support by Moffitt's Center of Excellence in Evolutionary Therapy.

Author contributions

M.F., R.R., and D.B. were responsible for computational model design, implementation, and analysis. S.B., Z.C., D.F., Y.-H.F., J.R.A., L.X.T.N., J.I., Y.-H.K., D.O., B.Z., and G.M. contributed to conception, experimental design, data generation, and/or data analysis. M.F., R.R., and D.B. were involved in the overall concept and design. R.R. and D.B. were involved in overall study supervision. All authors contributed to manuscript writing and editing.

Competing interests

The authors declare no competing interests.

Additional information

Supplementary information The online version contains supplementary material available at https://doi.org/10.1038/s41540-026-00675-6.

Correspondence and requests for materials should be addressed to Matthew Froid or David Basanta.